High-Misalignment Tolerance and Output Adjustable Wireless Charging System via Detuned Series–Series Compensated Reconfigurable Transmission Channels

Zhenjie Li, *Member, IEEE*, Jiafang He, Yusheng Huo, Mingfei Ban, *Member, IEEE*, Yiqi Liu, *Member, IEEE*, and Jiuqing Liu

***Abstract*—This article proposes a wireless charging system (WCS) with two reconfigurable transmission channels to achieve constant current/voltage (CC/CV) charging, anti-misalignment solid ability, and zero voltage switching (ZVS) operation. First, the structure design and working principle of the orthogonal magnetic coupler (OMC) are given. The OMC's parameters are optimized using the orthogonal experimental design. Then, the coupling performance of OMC is illustrated by Ansys simulations. Second, the topology and principle of the designed WCS are analyzed. The relationship between charging controllability, misalignment performance, and system parameters is presented. The design method and working principle of the magnetic flux controllable inductor (MFCI) used as the power adjustment circuit and auxiliary improvement of anti-misalignment ability are provided. Third, the schematic diagram and hardware of the closed-loop controller are given. The PLECS simulations verify the feasibility of using the MFCI to realize the above design goals. Finally, an experimental prototype of an unmanned aerial vehicle (UAV) is built to validate the method's feasibility. When the maximum charging power is 126 W, the maximum system efficiency is 91.6%. Besides, assuming system efficiency decreases by 5% from the maximum value, the maximum horizontal misalignment ratio is 42%, corresponding to a desired approximately circular charging region.**

***Index Terms*—Constant current/voltage (CC/CV) charging, misalignment performance, orthogonal magnetic coupler (OMC), reconfigurable circuit topology, wireless power transfer (WPT).**

I. Introduction

WIRELESS charging system (WCS) can transfer energy from the transmitter module to the receiver module without a direct electrical connection. It can be applied in many applications that use lithium batteries as an energy-storing unit, such as portable devices, uncrewed aerial vehicles (UAVs), automatic guided vehicles (AGVs), and electric vehicles (EVs) [1], [2], [3]. Hence, constant current (CC) and constant voltage (CV) charging is usually preferred to charge the battery. However, the variation in the battery's equivalent load resistance during the charging process influences system performance, such as the charging controllability and system efficiency. Besides, due to the receiver position's randomness, the WCS usually requires an anti-misalignment solid ability to maintain a desired system performance. Hence, this article's core purpose is to solve the above problems vital for the practicality of WCS.

A. Existing Relevant Research Works

Multiple methods to realize CC/CV charging for WCS, such as compensation topologies with load-independent output and closed-loop control methods, are proposed by many studies. The drawbacks of using compensation topologies to realize the approximate CC/CV charging are shown below: many passive components increase extra power loss and volume of WCS; the charging performance is easily influenced by system parameter variation; the charging controllability is limited once system parameters are fixed; the parameter design of compensation topology is usually complex [4], [5], [6], [7], [8]. Hence, primary-side and secondary-side closed-loop control strategies achieve CC/CV charging. Generally, the active rectifier and dc–dc converter are used for secondary-side control by adjusting the phase shift angle and duty cycle [9], [10], [11]. However, those methods induce extra power loss, weight, cost, and control complexity for the receiver. Hence, the primary-side control methods, realized by dc–dc converters and controllable inverters, are proposed as a remedy. However, these methods usually cannot achieve both CC/CV charging and zero voltage switching (ZVS) [12], [13], [14]. Then, some methods are proposed to solve this problem. First, a dc–dc converter with the variable frequency inverter (called a two-stage structure); second, a variable frequency with the phase shift controlled inverter (called a one-stage structure) [15]. Because the operating frequency changes dynamically, the above two methods may induce systematic instability.

Manuscript received 15 January 2023; revised 10 April 2023 and 17 May 2023; accepted 26 May 2023. Date of publication 31 May 2023; date of current version 1 September 2023. This work was supported in part by the National Natural Science Foundation of China under Grant 52107001, in part by China Postdoctoral Science Foundation under Grant 2022M710641, and in part by the Fundamental Research Funds for the Central Universities under Grant 2572021BF04. Recommended for publication by Associate Editor F. Lu. *(Corresponding author: Zhenjie Li.)*

Zhenjie Li, Jiafang He, Yusheng Huo, Mingfei Ban, and Yiqi Liu are with the College of Computer and Control Engineering, Northeast Forestry University, Harbin 150040, China (e-mail: lizhenjie0725@163.com; hejiafang_150000@nefu.edu.cn; h2054926990@nefu.edu.cn; banmingfei@nefu.edu.cn; nefukzc@nefu.edu.cn).

Jiuqing Liu is with the College of Mechanical and Electrical Engineering, Northeast Forestry University, Harbin 150040, China (e-mail: nefujdljq@163.com).

Color versions of one or more figures in this article are available at https://doi.org/10.1109/TPEL.2023.3281721.

Digital Object Identifier 10.1109/TPEL.2023.3281721

Generally, a fixed system operating frequency is preferred for the WCS to avoid bifurcation phenomena and obey some regulations, such as SAE J2954 for EVs wireless charging and WPC Qi for mobile phones. Hence, some methods are used to solve this problem. On the one hand, the controllable capacitor realizes CC/CV charging and ZVS operation [16]. On the other hand, the variable inductor (VI), whose equivalent inductance is altered by dc in its auxiliary winding, extends the ZVS operation range [17], [18]. However, this type of VI, which may suffer a nonlinear and limited adjustment range, is not aimed at realizing both CC/CV charging and ZVS operation. Hence, this article uses the magnetic flux controllable inductor (MFCI), which has a wide and linear adjustment range to realize both CC/CV charging and ZVS operation [19]. Besides, this paper further illustrates the MFCI's structure/parameter design and working principle, an improvement work for [19].

Moreover, misalignment is inevitable. Generally, the WCS is desired to have a horizontal anti-misalignment solid ability, while the vertical direction may not be strict [20]. Then many works propose various solutions to solve this problem.

1) *Magnetic Coupler:* Different types, such as the double D (DD) pad, double D quadrature (DDQ) pad, bipolar (BP) pad, and tripolar pad, are optimized to get a relatively uniform magnetic field distribution [21], [22], [23]. Besides, some magnetic couplers with hybrid coil structures have a better anti-misalignment ability, such as the combined solenoid and DD coils, overlay of quadruple-D and square coils, and a third-coil in reverse series with the primary coil [24], [25], [26], [27]. However, these magnetic couplers may still suffer problems, such as a limited misalignment tolerance range and complex parameter optimization.
2) *Compensation Topology*: The strong anti-misalignment ability is achieved by optimizing structure and parameters. First, the high-order compensation topologies, such as the S/SP and PS/P, are presented [25], [28]. Second, various hybrid compensation topologies, such as the combined SS with LCC and the combined S-LCC with LCC-S, are given [29], [30], [31]. Third, detuned compensation topologies, such as SS and LCC-S, are designed [32], [33]. Fourth, the dual-frequency compensation topologies, such as using the fundamental and third-order harmonic frequency to transfer power, are used in paper [34]. However, these methods may use many passive components, induce extra power loss, and need complex structure/parameter design.
3) *System-level Design:* Multiple circuits and closed-loop control strategies ensure a stable output power against misalignment. In [20], a μ-controller is designed to obtain robust power control when misalignment occurs. In [35], the misalignment-tolerant fractional-order WCS is given. A primary side DC-DC converter adjusts the output power when misalignment occurs [14]. The WCS with multiple transmission channels also ensures high-misalignment tolerance. In [36], the WCS features the one-to-multiple ability to achieve the goal of free positioning. In [37], the multichannel WCS with compact receivers for the UAV is designed to improve transmission stability and capacity.

Besides, some reconfigurable WCSs also realize much better anti-misalignment ability. A reconfigurable capacitive coupler, whose transmitters are activated by the UAV landing position, achieves stable coupling performance [38]. A dual-transmitter EV wireless charging system with reconfigurable topologies (SS and LCCC-S) has a high misalignment-tolerant ability [39]. The reconfigurable rectifier-based detuned SS-compensated IPT system to resist an extensive coupling range with relatively high efficiency is proposed in [40].

B. Main Works and Contributions

This article designs a reconfigurable WCS, which uses the combined orthogonal magnetic coupler (OMC) and MFCI to realize CC/CV charging, high anti-misalignment ability, and ZVS operation simultaneously even when mutual inductance and equivalent load resistance vary, which is less studied by existing work of the WCS. Furthermore, this article's research motivations and contributions are listed as follows.

1) The OMC with a lightweight receiver optimized by the orthogonal experimental design and Ansys simulations realizes a relatively smooth mutual inductance variation even when large horizontal misalignment occurs, ensuring a stable output power.
2) The topology and principle of the reconfigurable WCS are provided, especially the detailed analysis of the MFCI. The strategy for selecting a suitable transmission channel is also given to support the OMC's feasibility.
3) The primary-side MFCI uses the dual-loop PI controller to achieve CC/CV charging and ZVS operation. Besides, it assists in improving anti-misalignment ability. Then, the simulations and experiments verify the proposed method.

The rest of this article is organized as follows. Section II analyzes the structure and misalignment performance of the OMC; Section III designs the WCS and illustrates the working principle. Section IV analyzes the closed-loop control strategy and verifies it through simulation results. Section V builds the experimental prototype and validates the proposed method. Finally, Section VI concludes this article.

II. Analysis and Optimization of the Proposed OMC

A. Independent Structural Analysis of the OMC

As shown in Fig. 1, the transmitter in the OMC consists of two reverse series square (RSS) coils (the currents in two adjacent sides along the y-axis are opposite), different from DD coils (the currents in two adjacent sides along the y-axis are the same). The ferrite cores are placed below RSS coils to enhance the coupling performance. The receiver uses the square (S) coil and no ferrite cores to achieve the lightweight requirement. Although the transmitter's magnetic field with the RSS coils is relatively weak compared to the one with the DD coils, it has a higher x-direction misalignment tolerance, illustrated by Fig. 2.

When the receiver with an S coil is used, some transmitters with different coil structures are compared with the RSS coils. Fig. 2 indicates that the magnetic coupler with the RSS coils (transmitter) and S coil (receiver) has the best x-direction

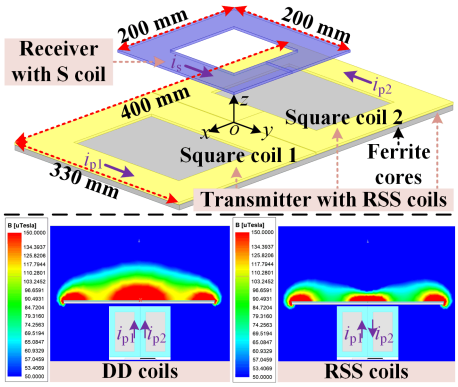

Fig. 1. Analysis of the magnetic coupler with the RSS coils (transmitter) and S coil (receiver).

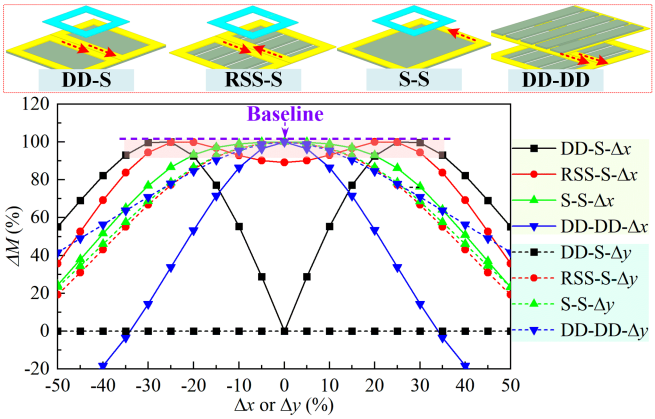

Fig. 2. Performance comparison of some different magnetic couplers.

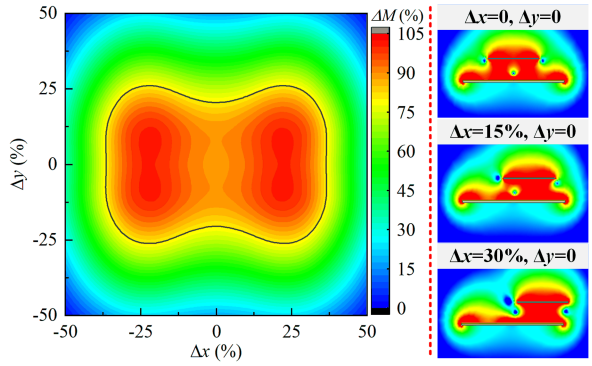

Fig. 3. Misalignment performance of the magnetic coupler with the RSS coils (transmitter) and S coil (receiver).

anti-misalignment ability. Besides, the magnetic coupler with dual-side DD coils is also compared to ensure the comparison's feasibility.Δx is the x-direction misalignment distance ratio to the coil width; Δy has the same definition. ΔM is the absolute ratio of different positions' mutual inductance to the maximum values marked by the baseline.

Fig. 3 shows that the magnetic coupler with the RSS coils (transmitter) and S coil (receiver) features a relatively smooth fluctuation of ΔM within the area surrounded by the black line.

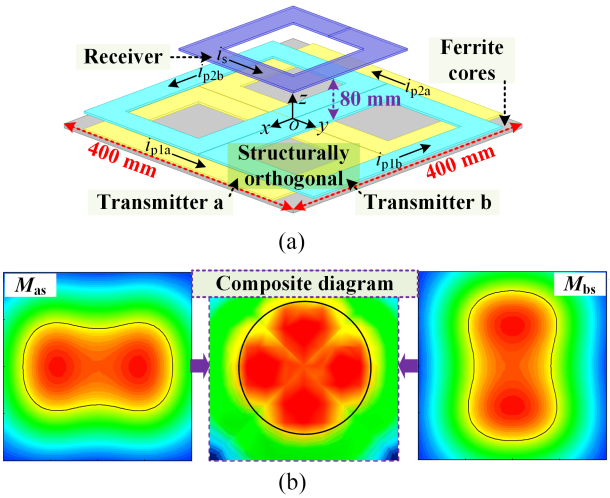

Fig. 4. Analysis of the OMC. (a) Structure and dimensions. (b) Horizontal misalignment performance.

Moreover, the x-direction misalignment performance is much better than the y-direction, which laid the foundation for this paper's OMC proposal. It consists of two transmitters placed in the orthogonal structure or with an angle of 90°(take the central axis as a reference) to build a uniform magnetic field for the receiver when horizontal misalignment occurs. Furthermore, the OMC is analyzed and optimized in Section II-B.

B. Structure and Principle Analysis of the OMC

Combining the above analysis, the OMC is plotted in Fig. 4(a). The dimensions of two transmitters and one receiver are the same as in Fig. 1. The ferrite cores are enlarged to cover two transmitters. The mutual inductances between the transmitters and the receiver are $M_{\rm as}$ and $M_{\rm bs}$ for transmission channel I and II. Fig. 4(b) shows that the fluctuation of $M_{\rm as}$ is smooth in the x-direction, while the change of $M_{\rm bs}$ is smooth in the y-direction. Then, the OMC combines these two advantages and ensures a smooth mutual inductance fluctuation within the horizontal misalignment area marked by a composite diagram.

The OMC's principle is further illustrated as follows. When horizontal misalignment occurs, the transmission channel with a larger mutual inductance works; the other is in an open circuit state. Then, the misalignment problem of some usually used magnetic couplers corresponding to the significant reduction in mutual inductance can be mitigated. Because only the activated transmitter works, the cross-mutual inductance $M_{\rm ab}$ between two transmitters does not influence the system performance. Besides, the circuit structure and control strategy used to realize the transmission channel selection are analyzed in Section III.

C. Optimization of the OMC Using Orthogonal Experimental Design

One of the main goals for designing the OMC is to achieve the desired maximum misalignment tolerance. The orthogonal experimental design, which selects some representative points from the comprehensive test based on the orthogonality, and

TABLE I
MAIN PARAMETERS OF THE DESIGN WCS

Symbol	Parameter note	Values
U_{bus}	System input direct voltage	150 V
f	System operating frequency	85 kHz
L_{pa}	Self-inductance of the transmitter coil a	317 μH
L_{pb}	Self-inductance of the transmitter coil b	285 μH
L_s	Self-inductance of the receiver coil	74 μH
M_{as}&M_{bs}	Mutual inductance of the OMC when no misalignment occurs	18.6 μH &18.5 μH
M_{ab}	Mutual inductance between two transmitters of the OMC	116 μH
U_{o_range}	Battery operating voltage range	16 V~25.2 V
I_{o_set}	Preset constant charging current	5 A
R_o	Equivalent load resistance of the battery	3.2 Ω~50 Ω
U_{dc}	Input direct voltage for the MFCI	150 V
L_{av}&L_{bv}	Self-inductance of the transformer in the MFCI	75 μH & 75 μH
M_{abv}	Mutual inductance of the transformer in the MFCI	60 μH
L_{cv}&C_{cv}	The inductance and capacitance of the filter in the MFCI	75 μH & 46.8 nF

the Ansys Maxwell software, which realizes the simulations of multiple parameter sweeps, optimize the OMC's coil turns. The main implementation steps are illustrated as follows. First, determine the design parameters and each factor's level number. Second, design the orthogonal experimental table and use the Ansys Maxwell simulations to obtain the orthogonal experimental results. Third, the simulation results are analyzed, and the best parameter combination is selected according to the design goal. Finally, the final simulation result uses the optimal parameter combination and is compared with the initial design parameters to verify the results' feasibility.

Combined with the system parameters in Table I, the detailed OMC design process is listed in the Appendix. It shows that the optimized OMC's coil turns are 15 for two transmitters and 16 for the receiver. The Litz wire diameter is about 2.4 mm (0.05 mm & 1000). The ferrite cores' material and size are PC95 and 400 mm × 400 mm × 2.5 mm. Then, the orthogonal table and test results can analyze the theoretical value under any parameter level combination to achieve the most favorable parameter combination. The orthogonal experimental design can also be used to optimize other parameters of the OMC, such as size and structure. Besides, it may also suit different magnetic couplers and compensation topologies in the WCS.

The mutual inductance M_{ps} shown in Fig. 5 further verifies the rationality of the optimized OMC. For example, when the fluctuation of M_{ps} is 5%, the black line surrounds the available horizontal misalignment region. Note: only the maximum M_{ps} of two transmission channels are recorded at the fixed position, corresponding to the OMC's principle.

III. SYSTEM STRUCTURE AND THEORETICAL ANALYSIS

First, the structure of the reconfigurable WCS is analyzed. Second, the influence of system parameters on the charging current/voltage and misalignment performance is illustrated. Third, the working principle of the WCS is analyzed, especially the mode selection strategy for activating a proper transmission

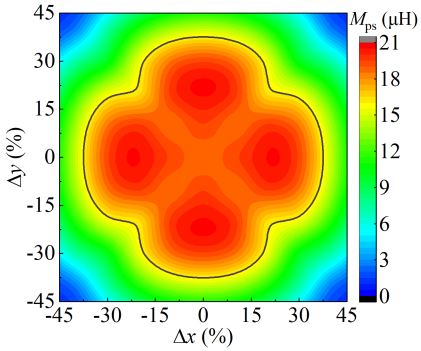

Fig. 5. Horizontal misalignment performance of the OMC.

channel. Finally, the parameter design method for the MFCI is given to ensure high system working performance.

A. Circuit Structure Analysis

As shown in Fig. 6, the WCS consists of two primary-side transmission channels that cannot be activated simultaneously. Primary-side transmission channel I contain the below parts: an improved half-bridge inverter with three MOSFETs (Q_{a1} and S_a; S_a consists of Q_{a2} and Q_{a3} in reverse series connection, blocking the current in transmission channel II when it stops working), a transmitter (coil inductance and resistance are L_{pa} and R_{pa}), a compensation capacitor (capacitance and resistance are C_{pa} and R_{ca}). The MFCI consists of the following parts: a full-bridge inverter (MOSFETs Q_a–Q_d); an LC filter (L_{cv} and C_{cv}); a transformer (L_{av} connected in series with the WCS, L_{bv} joined in parallel with L_{cv}), a current transformer (CT_{av}), and the control unit. A detailed analysis of the MFCI is shown in Section III-D.

On the secondary side, L_s and R_s are the inductance and resistance of the receiver coil; C_s and R_{cs} are the capacitance and resistance of the compensation capacitor. Four diodes and a capacitor (D_1–D_4 and C_o) form the rectifier with a capacitive filter. U_{bus} is the input voltage for the WCS; the output voltages of two inverters are u_{pa} and u_{pb}. The resonant currents in two transmitters are i_{pa} and i_{pb}. The resonant current in the receiver is i_s. The rectifier's input voltage and resistance are u_e and R_e. R_o is the battery's equivalent load resistance. I_o and U_o are the charging current and voltage. Then, they are measured by the current/voltage sensors and transferred to the primary-side controller for CC/CV charging and mode selection.

B. Equation Deduction and Theoretical Analysis

The below assumptions simplify the equation deduction.

1) The fundamental harmonic approximation (FHA) approach is applied because the frequency selection characteristic of the resonant tank can suppress the high-order harmonics [41].
2) Two improved half-bridge inverters operate at the resonant frequency of SS compensation with a fixed duty cycle.
3) L_p represents the L_{pa} or L_{pb} used; a similar definition applies to other symbols.

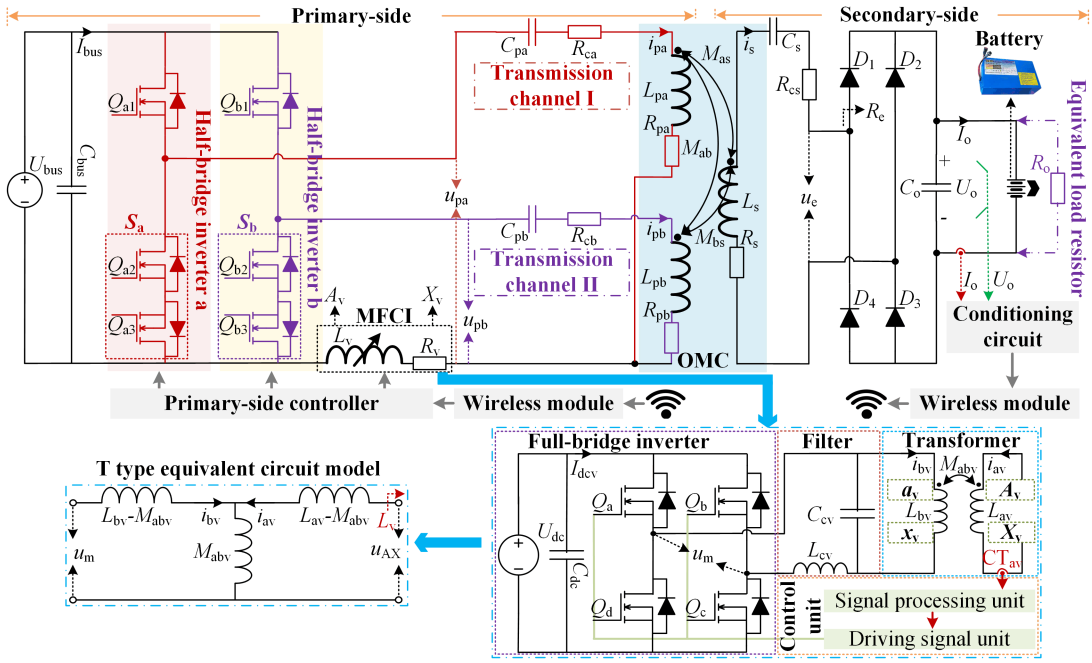

Fig. 6. Circuit structure of the proposed WCS.

4) The battery is assumed to be an equivalent load resistor R_o because its charging process is much smaller than the system's working period [42].

The relationships among R_e, R_o, I_s, I_o, U_{bus}, and U_p are given by (1). Here, the root-mean-square (RMS) values of i_s and u_p are I_s and U_p

$$R_e = \frac{8}{\pi^2}R_o, I_o = \frac{2\sqrt{2}}{\pi}I_s, U_p = \frac{\sqrt{2}}{\pi}U_{bus}. \tag{1}$$

When one transmission channel works, the secondary-side and primary-side impedance are deduced as follows:

$$Z_s = \underbrace{j\omega L_s + \frac{1}{j\omega C_s}}_{0} + \underbrace{R_s + R_{cs}}_{R_2} + \frac{8}{\pi^2}R_o \tag{2}$$

$$Z_p = \underbrace{j\omega L_p + \frac{1}{j\omega C_p}}_{0} + \underbrace{R_v + R_c + R_p}_{R_1} + j\omega L_v + \frac{(\omega M_{ps})^2}{Z_s}. \tag{3}$$

Based on (1)–(3), I_o is given by (4) and verified by Fig. 7. When R_o and M_{ps} vary, I_o or U_o is regulated by L_v. This point provides theoretical support for CC/CV charging through the closed-loop controller, analyzed in Section IV. Besides, the difficulty of controlling I_o or U_o is further alleviated using the OMC, which has a relatively smooth fluctuation of M_{ps} within a suitable horizontal misalignment region, as shown in Fig. 5

$$I_o = \frac{4U_{bus}(\omega M_{ps})}{\sqrt{[\omega L_v A]^2 + \left[R_1 A + (\omega M_{ps}\pi)^2\right]^2}}, A = 8R_o + R_2\pi^2. \tag{4}$$

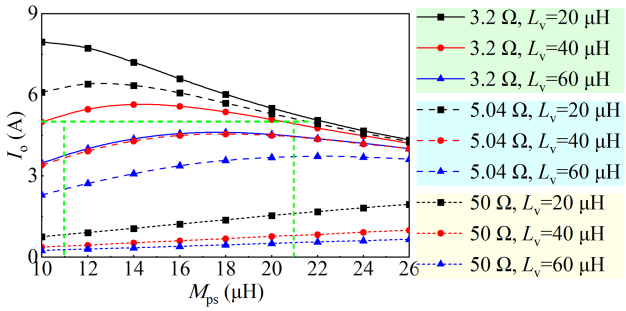

Fig. 7. Simulation results of I_o versus M_{ps} under different L_v and R_o.

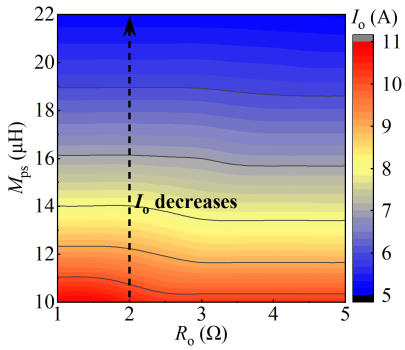

Fig. 8. Simulation results of I_o versus R_o and M_{ps}.

C. Working Principle of the Proposed WCS

As shown in Fig. 8, when L_v is 10 μH, and R_o is a fixed value, the larger the M_{ps} is, the smaller the I_o is. For example, the dashed line shown in Fig. 8. This conclusion lays the theoretical foundation for achieving mode selection that is realized by only

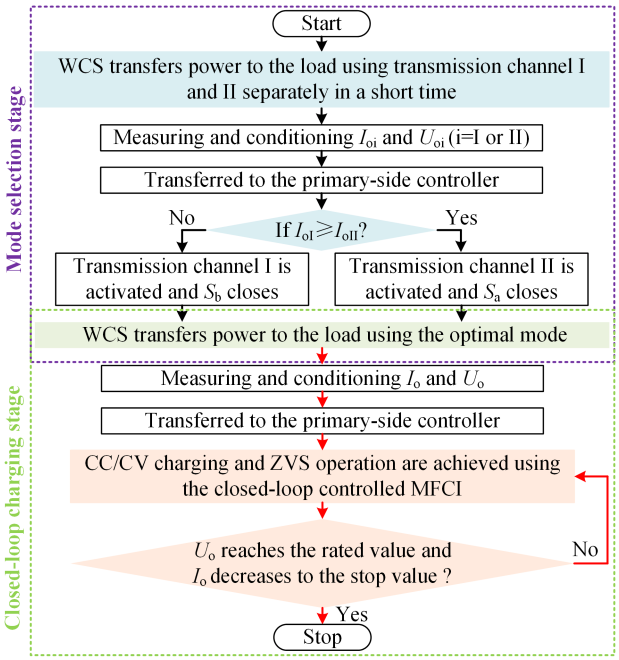

Fig. 9. Working principle block diagram of the proposed WCS.

measuring I_o and U_o. Combing the circuit in Fig. 6, the working principle block diagram of the WCS is further illustrated in Fig. 9. It consists of the mode selection and closed-loop charging stages. For the first stage, two transmission channels, I and II, which cannot be activated simultaneously, supply power to the load separately for a short time. Then, the measured I_o and U_o are transferred to the primary-side controller and compared. Then, the transmission channel that achieves the smaller I_o is activated for the second stage. This mode selection method does not require complex hardware that some existing research may usually use, which helps reduce the complexity of the WCS. For the second stage, the closed-loop controlled MFCI realizes CC/CV charging and ZVS operation using the I_o and U_o transferred from the secondary side. Also, it helps improve the anti-misalignment ability analyzed in Section IV-B. Finally, the WCS stops working when stop-charging conditions are met.

D. Analysis of the MFCI for CC/CV Charging

Based on the system design goals, the MFCI's transformer is optimized using a similar design method for the OMC. Then, the dimensions are plotted in Fig. 10(a). The coil turns of L_{av} and L_{bv} are 14 (7 turns for one layer, totaling two layers). The parameters design of the MFCI is analyzed in the Appendix. Unlike the usually used transformer, the one used by the MFCI is double-side excited by i_{av} and i_{bv} with a phase difference of 180°, as shown in Fig. 10(a). Besides, the working principle of the MFCI is further illustrated using the T-type equivalent circuit model plotted in Fig. 6.

Assuming the transformer in the MFCI works without load, the no-load magnetic potential is expressed as (5). Then, the main magnetic flux generated by this magnetic potential further

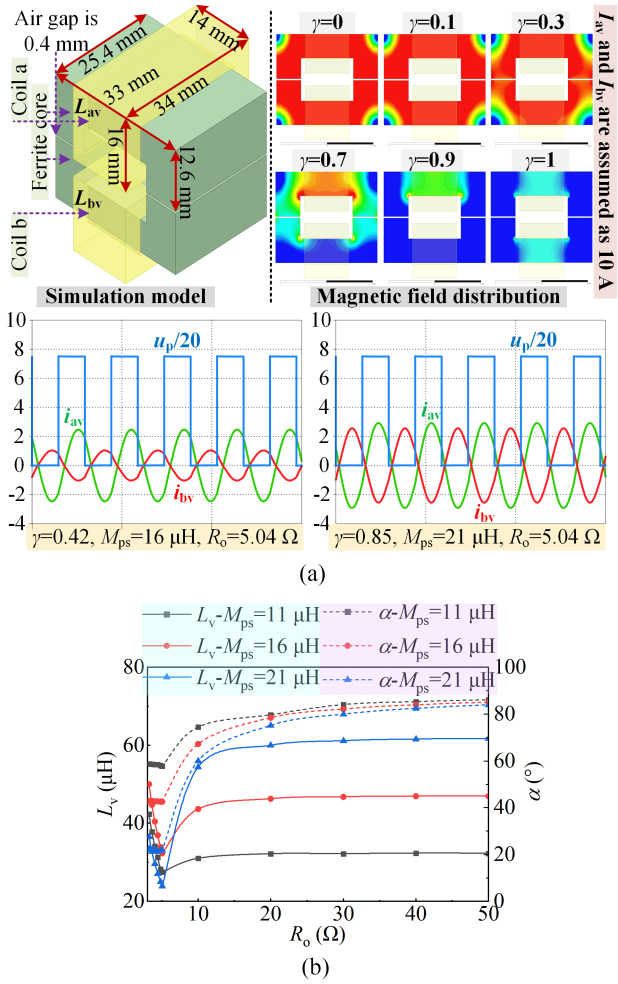

Fig. 10. Analysis of the MFCI. (a) Model, magnetic field distribution, and waveforms. (b) L_v and α versus R_o.

generates an induced electromotive force between A_v and X_v and is given by (6). W_{av} and W_{bv} are the transformer's primary- and secondary-side coil turns

$$\dot{F}_{AX} = W_{av}\dot{I}_{av} \tag{5}$$

$$\dot{E}_{AX} = -j4.44fW_{av}\dot{\Phi}_{mN} = -j\omega M_{abv}\dot{I}_{av}. \tag{6}$$

The KVL equation between A_v and X_v is expressed as follows:

$$\dot{U}_{AX} = j\omega\left(L_{av} - M_{abv}\right)\dot{I}_{av} - \dot{E}_{AX}. \tag{7}$$

When the current meets (8) and is actively injected into the port a_v, the transformer's total magnetic potential is given by (9). Then, the main magnetic flux is expressed $(1-\gamma)\dot{\Phi}_{mN}$ and verified by the magnetic field distribution shown in Fig. 10(a). Finally, an induced electromotive force between A_v and X_v is generated and given by (10)

$$\dot{I}_{bv} = -\gamma\dot{I}_{av}, \gamma \in (0,1) \tag{8}$$

$$\dot{F}_T = W_{av}\dot{I}_{av} + W_{bv}\dot{I}_{bv} = (1-\gamma)W_{av}\dot{I}_{av} \tag{9}$$

$$\dot{E}_{\mathrm{AX}} = -j4.44 f W_{\mathrm{av}} (1-\gamma)\, \dot{\Phi}_{\mathrm{mN}} = -j\omega M_{\mathrm{abv}} (1-\gamma)\, \dot{I}_{\mathrm{av}}. \tag{10}$$

The L_{v} is given by (11). Besides, the relationship between the adjustable L_{v} and the desired I_{o} or U_{o} is deduced as (12) and further validated by Fig. 10(b). Here, the desired I_{o} is set as 5 A

$$\begin{aligned} \dot{U}_{\mathrm{AX}} &= j\omega \left(L_{\mathrm{av}} - \gamma M_{\mathrm{abv}}\right) \dot{I}_{\mathrm{av}} = j\omega L_{\mathrm{v}} \dot{I}_{\mathrm{av}} \\ &\Rightarrow L_{\mathrm{v}} = L_{\mathrm{av}} - \gamma M_{\mathrm{abv}} \in \left[L_{\mathrm{av}} - \gamma M_{\mathrm{abv}}, L_{\mathrm{av}}\right] \end{aligned} \tag{11}$$

$$L_{\mathrm{v}} = \frac{1}{\omega A I_{\mathrm{o}}} \sqrt{\left[4 U_{\mathrm{bus}} \omega M_{\mathrm{ps}}\right]^2 - \left[R_1 A I_{\mathrm{o}} + (\omega M_{\mathrm{ps}} \pi)^2 I_{\mathrm{o}}\right]^2}. \tag{12}$$

The MFCI can also provide an inductive impedance for the inverter, and the phase difference α between u_{p} and i_{p} is given by (13) and further verified by Fig. 10(b). In general, the ZVS operation helps reduce the switching loss of the MOSFETs. Then, it proves that the MFCI simultaneously realizes CC/CV charging and ZVS operation compared with some existing primary-side circuits and control methods

$$\alpha = \arctan \frac{\omega L_{\mathrm{v}} A}{A R_1 + (\omega M_{\mathrm{ps}} \pi)^2} > 0. \tag{13}$$

IV. Closed-Loop Controller and Simulation Analysis

First, the schematic diagram and hardware of the closed-loop controller are analyzed. Second, the simulation results from PLECS software verify the feasibility of using the closed-loop controlled MFCI to realize CC/CV charging, ZVS operation, and auxiliary improvement of the anti-misalignment ability.

A. Closed-Loop Controller Analysis

The control diagram of the WCS is shown in Fig. 11(a).

The control diagram mainly consists of mode selection and closed-loop charging—first, the I_{o} and U_{o} are used to activate the suitable transmission channel with a larger M_{ps} to ensure high system working performance. Second, the WCS operates in charging mode, and the I_{o} and U_{o} are sent to the primary side. On the one hand, the transformer in the MFCI acquires i_{av}; then, it is processed into the triangular wave and compared with γ to generate driving signals for the full-bridge inverter in the MFCI. On the other hand, the dual-loop PI controller, which comprises an inner charging current loop (I) and an outer charging voltage loop (II), generates γ for the MFCI to realize CC/CV charging and ZVS operation.

Furthermore, loop (II) does not work when the WCS works in CC charging mode; it is equivalent to a single-loop control. When the WCS works in CV charging mode, it adopts cascade control; loop (I) is the inner loop of the voltage loop; the output of loop II is used as a reference signal for loop I. Compared with two independent controllers, the dual-loop PI controller can solve the current limiting problem and has a faster current limiting response speed. Besides, Fig. 11(b) shows the designed hardware for the closed-loop control. The control board realizes the mode selection and closed-loop charging; the signal board completes the signal acquisition, conditioning, and processing. The closed-loop simulations further verify the above analysis.

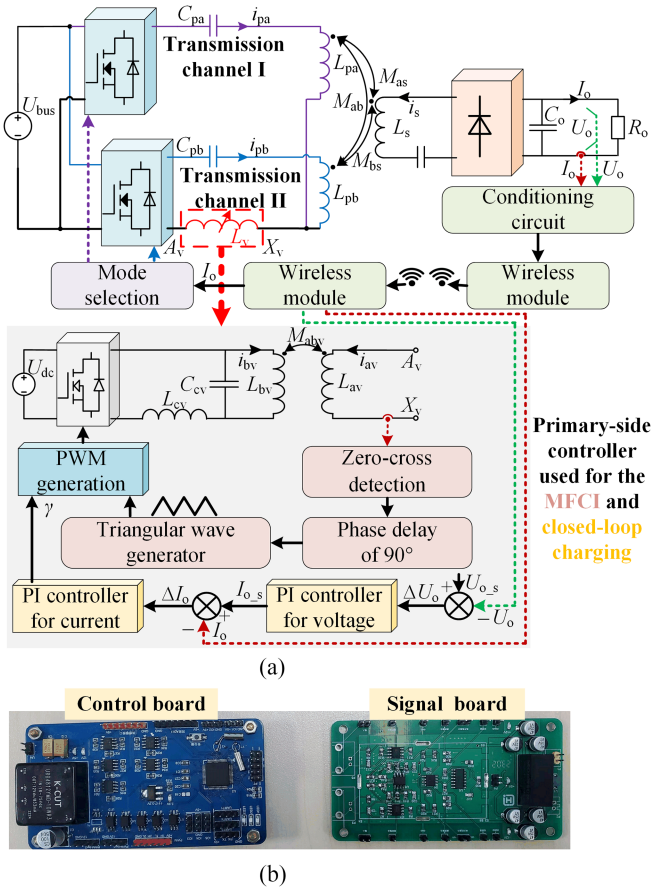

Fig. 11. Closed-loop controller analysis. (a) Schematic diagram. (b) Hardware.

B. Closed-Loop Simulation Analysis

When M_{ps} and R_{o} vary, Fig. 12 shows that adjusting L_{v} of the closed-loop controlled MFCI realizes CC/CV charging and ZVS operation. Fig. 13(a) shows that the closed-loop controller has a relatively wide range of regulation abilities. Fig. 13(b) shows that system efficiency η can still maintain high during CC charging when large misalignment occurs, corresponding to R_{o} of 3.2 to 5.04 Ω.

Besides, the misalignment performance comparison of using the designed closed-loop controller or not is shown in Fig. 14. Here, CC charging is 5 A (the pink dash line), and CV charging is 25.2 V (the purple dash line). Besides, other R_{o} shares a similar conclusion as below.

Take one scenario in Fig. 14: when R_{o} is 5.04 Ω, Δy is 0, and the fluctuation of I_{o} is 1%, the available Δx for open-loop working is 8%. In contrast, the available Δx for closed-loop working is larger than 40%. Hence, the feasibility of using the MFCI to improve the anti-misalignment ability is verified.

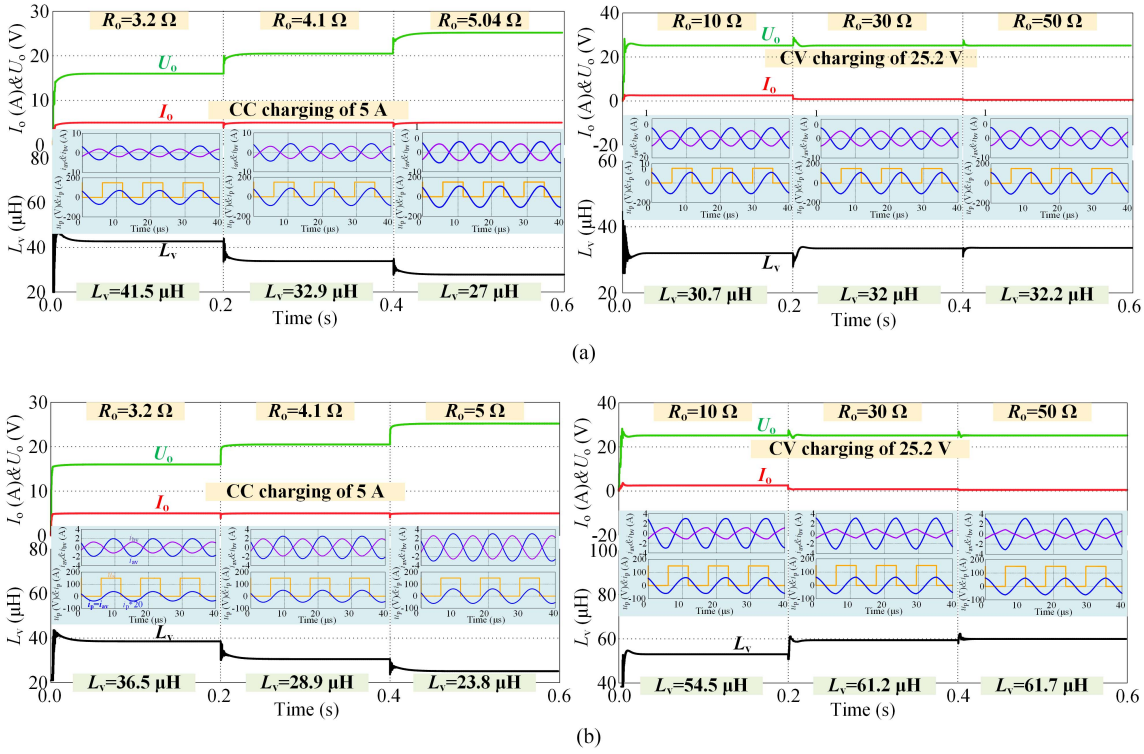

Fig. 12. The closed-loop simulation waveforms for CC/CV charging. (a) M_{ps} equal 11 μH. (b) M_{ps} equal 21 μH.

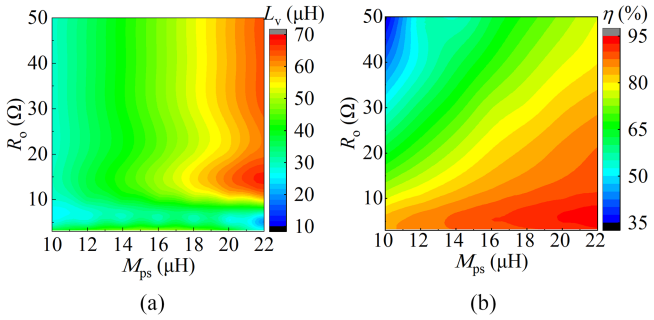

Fig. 13. Simulation results when M_{ps} and R_o vary. (a) L_v. (b) η.

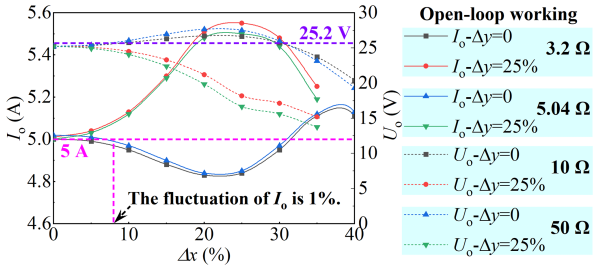

Fig. 14. Misalignment performance with/without using a closed-loop controller.

V. Experimental Validation

First, an experimental prototype with the maximum output power and system efficiency of 126 W and 91.6% used for the UAV is constructed. Second, the open-loop and closed-loop experimental results are given. Third, the proposed method is compared with some existing research works. Finally, a further discussion and future work of this paper are provided.

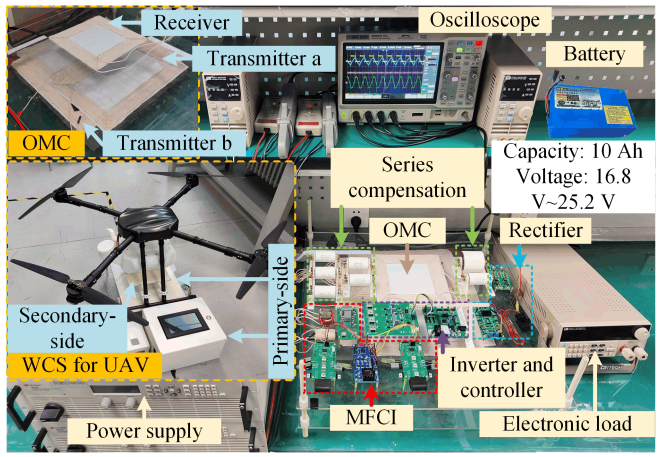

Fig. 15. Experimental prototype.

A. Experimental Prototype

The power level of the experimental prototype shown in Fig. 15 is selected based on the battery capacity of the existing UAV. A higher output power can be realized by adjusting the system parameters reasonably. On the primary side, one improved half-bridge inverter uses three MOSFETs (IPW60R017C7), one gate drive optocoupler (HCPL-3180), and one isolated dual-channel gate driver (UCC21520). The SS compensation uses

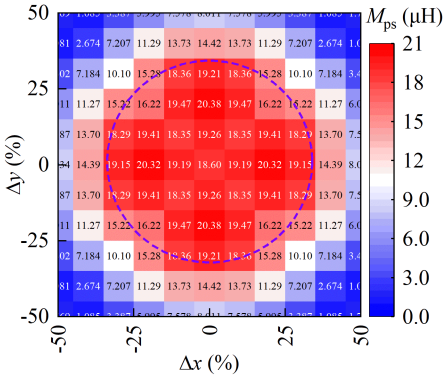

Fig. 16. Measured M_{ps} of the OMC when horizontal misalignment occurs.

the resonant capacitors from DAWNCAP. The full-bridge inverter in the MFCI uses the same MOSFET and driver as above. The primary-side controller uses STM32F405RGT6. On the secondary side, the rectifier consists of four Schottky diodes (NTST30120CT), and the filter uses nonpolar capacitors. The WiFi module (ATK-ESP8266) transfers charging information to the primary-side controller. The current and voltage sensors (HCS-ES3.3-10A and HVS-AS3.3.-10mA) measure I_o and U_o; Two current transformers (DBKCT16) obtain i_{av} and i_{bv}; The dc power supply and dc electronic load are N8944A from KEYSIGHT and IT8513C from ITECH. The digital power analyzer, WT1800 of YOKOGAWA, analyzes the power and efficiency of the WCS. The digital oscilloscope, SDS2204X of SIGLENT, collects waveforms. The LCR analyzer, IM3536 of HIOKI, measures the self and mutual inductances of the OMC.

B. Experimental Results Analysis

The M_{ps} are measured and plotted in Fig. 16. The region is approximately circular when M_{ps} vary less than 5%, consistent with the simulation results shown in Fig. 5.

Fig. 17(a) verifies that the phase angle between i_{av} and i_{bv} is 180°, and different L_v measured in Fig. 17(b) is obtained by adjusting γ or the full-bridge inverter's phase-shift angle. For example, when γ is 0.36, the measured $L_{v\text{-}m}$ is 52.8 μH, and the output power P_o is 75.2 W. Fig. 17(b) shows that the average error between $L_{v\text{-}m}$ and the calculated $L_{v\text{-}c}$ is less than 1% for the MFCI in this article. Besides, Fig. 17(b) shows that P_o, which corresponds to I_o or U_o, is regulated by changing L_v when R_o and M_{ps} vary, supporting the closed-loop control's feasibility.

Based on the above open-loop analysis, the closed-loop experimental results are given to verify the proposed method further. When R_o changes, and M_{ps} is 11 μH, Fig. 18 confirms that CC/CV charging and ZVS operation are achieved using the closed-loop controlled MFCI. This conclusion applies to other misalignment conditions, whose M_{ps} varies from 11 to 20.3 μH, further verified by Fig. 19(a). Besides, when R_o is 5.04 Ω, corresponding to the maximum output power P_{omax} and η decreases by 5% from its maximum value η_{max}, the black line shown in Fig. 19(b) surrounds the suitable charging zone for the WCS. Besides, other R_o shares a similar conclusion.

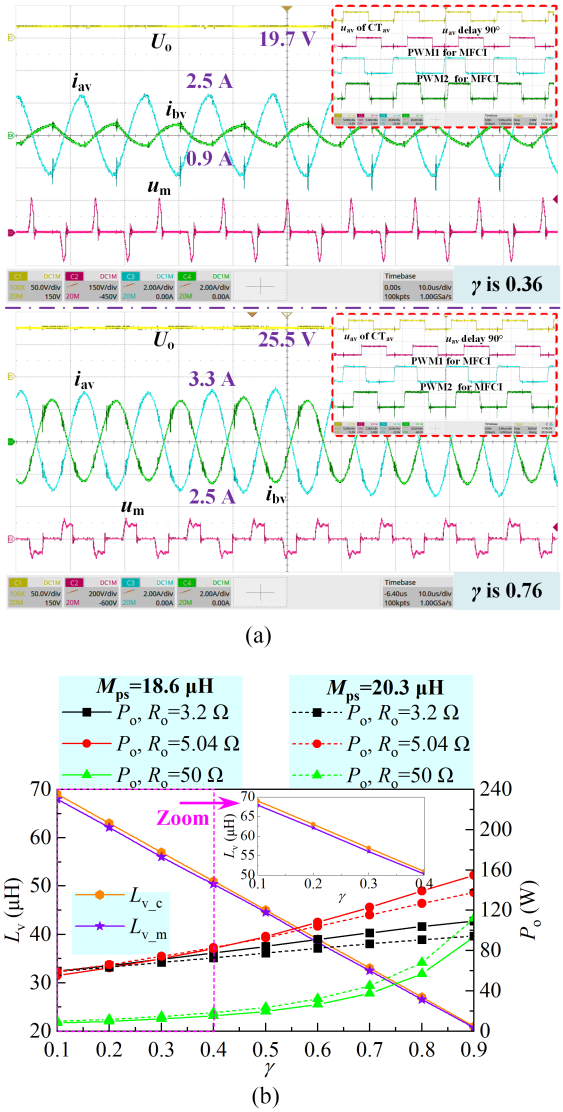

Fig. 17. Open-loop test of the MFCI. (a) Waveforms. (b) γ versus L_v and P_o.

As shown in Fig. 20(a), when R_o varies, η_{max} exists for the WCS at the transition point between CC and CV charging. Fig. 20(b) shows the power loss when the maximum and minimum M_{ps} occur. The average power proportion of MFCI in system input power is less than 1.3%, which may still be acceptable considering its multiple functions. Besides, the detailed power loss analysis of MFCI is shown in the Appendix to guide the efficiency improvement.

As shown in Fig. 21, the positive α confirms that an inductive impedance is ensured for the inverter to realize ZVS operation within the designed working range, reducing the switching loss.

C. Comparison With Existing Research Works

Compared with some related references in Table II, this article's method ensures a lightweight/simple receiver module and accurate CC/CV charging without sacrificing misalignment performance, which can be seen as an extension of the existing research. During the comparisons, the 5% mutual inductance

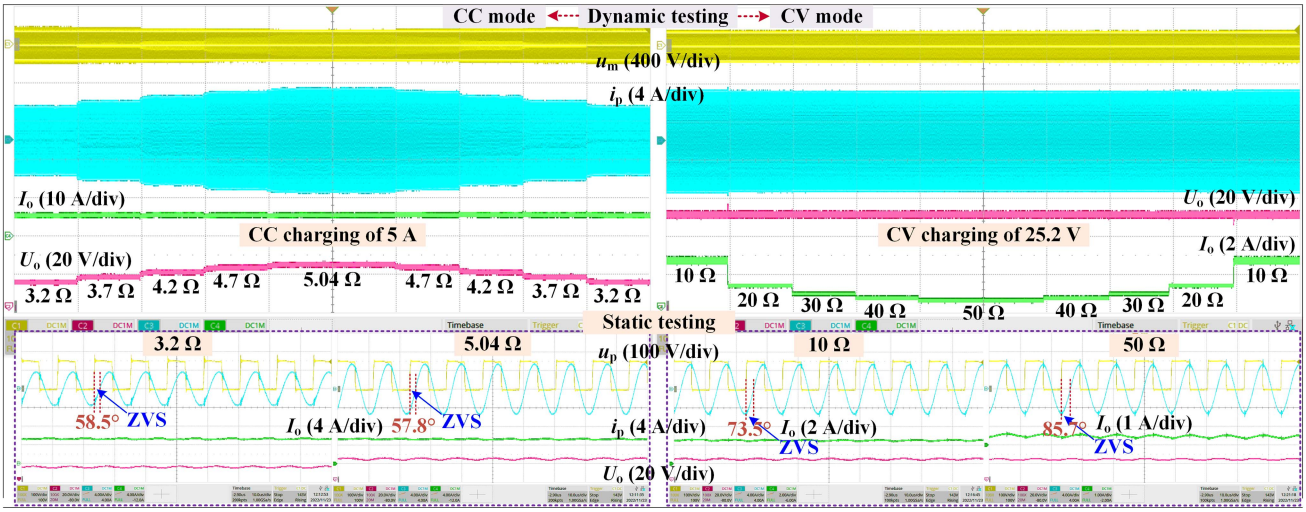

Fig. 18. Measured waveforms of CC/CV charging when R_o varies from 3.2 to 50 Ω. Note: x Ω represents the battery's equivalent load resistance.

TABLE II
COMPARISON TO SOME RELATING REFERENCES

Ref	Magnetic coupler size (unit: cm)	Mutual inductance fluctuates within 5%	Does the receiver use ferrite cores, and what's the coil type?	Output performance and load resistance (Ω)	Charging ability	Anti-misalignment method
[24]	Transmitter and receiver: 25*21	Δx: ±69% Δy: ±46%	Yes, series solenoid and DD coils (☹-complex)	310 W&91.2% (max) 50 Ω~200 Ω	Nearly CV	Magnetic coupler
[25]	Transmitter: 45*45, receiver: 40*40	Δx: ±40% Δy: ±40%	Yes, square coil	3.3 kW&96% (max) 15 Ω~34 Ω	Nearly CP	Magnetic coupler
[26]	Transmitter and receiver: 28*28	Δx: ±50% Δy: ±50%	Yes, square coil	200 W&81.2% (max) 5 Ω~15 Ω	Nearly CC	Compensation and magnetic coupler
[27]	Transmitter and receiver: 40*40	Δx: ±37% Δy: ±37%	Yes, quadruple-D quadrature coils (☹-complex)	3.5 kW&96% (max) 16 Ω~32 Ω	Nearly CV	Hybrid compensation and magnetic coupler
[31]	Transmitter and receiver: 40*40	Δx: ±50% Δy: ±13% (☹)	Yes, double-D quadrature coils (☹-complex)	1000 W&94% (max) 36 Ω~480 Ω	Nearly CC/CV	Hybrid compensation with receiver switchable circuit
[41]	Transmitter: 60*30, receiver: 30*30	Δx: ±42% Δy: ±33% (☹)	Yes, square coil	1.5 kW&96% (max) 30 Ω	Nearly CP	System topology
[46]	Transmitter: 20*20, receiver: 40*20	Δx: ±50% Δy: ±10% (☹)	Yes, square coil	100 W&94.1% (max) 40 Ω	Nearly CP	System topology
This work	Transmitter: 40*40, receiver: 20*20	Δx: ±37% Δy: ±37%	No, square coil (☺-simple)	126 W&91.6% (max) 3.2 Ω~50 Ω	Accurate CC/CV	System-level design from topology and control

fluctuation is the reference to test the magnetic coupler's performance. Although the OMC's misalignment performance is not the best, it still has the below advantages. For example, compared to the methods in [24], [27], and [31], the OMC has a simpler structure and is easier to be made. Compared with the methods in [25] and [26], the OMC's structural design and parameter optimization is much more convenient. Compared to the method in [40] and [20], the OMC performs better with comprehensive horizontal misalignment performance. As a remark, the total balance between structural complexity and coupling performance should be considered in designing the magnetic coupler. For example, if the receiver in the OMC uses ferrite cores, its anti-misalignment ability can be improved, but it goes against the lightweight demand.

Furthermore, the closed-loop controlled MFCI improves Δx and Δy to ±42%, as shown in Fig. 19. This method can also be used for these references to enhance their system performance. Note: considering various design goals, different magnetic couplers have their technological superiorities, which means a strictly fair comparison is not accessible. Hence, only some critical indicators related to this paper's work are compared. Besides, if the mutual inductance fluctuation within 5% is not applicable, the output variation of 5% is used as a substitute [31]. It is also pointed out that those comparisons are provided based on the literature analysis. Some results may be incomplete due to limitations in available data.

As a supplementary explanation, due to the designed WCS with a lightweight receiver having two transmission channels, some similar references are compared to verify its rationality. The design goals of these references can be roughly classified and analyzed as follows.

1) *Maximum Efficiency [43], [44], [45], [46]:* In [43], the transmitter coils selection for maximum power transfer efficiency is proposed for the WCS with multiple transmitter coils and a single receiver coil. However, it suffers from the following problems: the transmitters' cross-coupling effect should be solved, extra switches are required to select the activated transmitter, and poor anti-misalignment ability. In [46], an impedance-matching method is proposed to improve the system efficiency under horizontal misalignment conditions. However, it is used for fixed x-direction motion trajectory applications. When

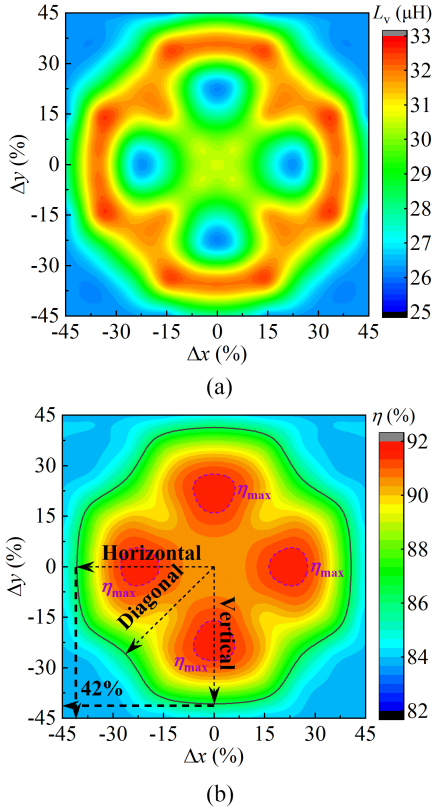

Fig. 19. Measured (a) L_v and (b) η when horizontal misalignment occurs.

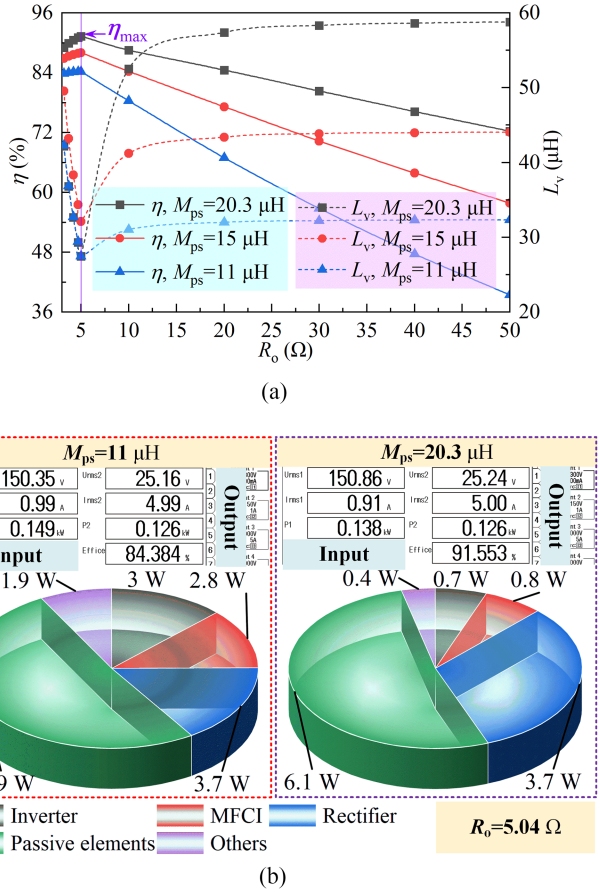

Fig. 20. Measured results with different R_o and M_{ps}. (a) η and L_v. (b) Power loss.

the y-direction misalignment occurs, it is not applicable. Note: the WCS designed in this article does not cover this goal, then no further analysis is provided.

2) *High Anti-misalignment Ability [2], [47], [48], [49]:* In [48], a quasi-uniform magnetic coupling-based configuration WPT system with multiple extended transmitter coils is proposed for UAV's wider-area charging. However, it may suffer the following problems: many ac switches that may induce additional power loss are required to realize the transmitter coil combinations, and an accurate position detection circuit is required. In [49], an efficient and robust free-positioning WPT system in a large area is proposed using an almost continuous magnetic flux path. However, it may suffer the following problems: many full-bridge inverters are used, the transmitter structure combined with the decoupling inductor is relatively complex, and the power balance problem should be considered. Note: Combined with these references' idea of multiple transmitters selection, the OMC with two switchable transmitters ensures better horizontal anti-misalignment ability.
3) *Power Balance and Current Sharing [50], [51], [52], [53]:* In [50], a simple and low-cost current-sharing method to balance the input power is proposed for the inductive power transfer system with multi transmitters. In [52], coupled inductors with a cyclic cascade connection instead of a complex controller are used to solve the unbalance current problem of the multiphase parallel resonant inverter with high output power. However, the power balance and current sharing problem among multiple transmitters do not exist in OMC because its two transmitters can not both work. Furthermore, these references provide an exciting idea that the two transmitters in OMC work simultaneously to ensure better system performance, which is the next research stage.

Based on the above analysis and the system design goals, the proposed two transmitters selection method for OMC, aimed to improve the system's horizontal anti-misalignment ability, is easily realized for the designed WCS using only the charging current/voltage and no complex circuits.

D. Further Discussion and Future Works

Furthermore, the following analysis help extend this article's research work.

1) Regarding the complex problem of the designed WCS, it is well known that the circuit units should be reasonably designed considering different design goals in developing a practical WCS. In other words, using only one circuit unit or control freedom to achieve more than two design goals may usually be challenging. For example, suppose this paper desires only CC/CV charging; the MFCI can realize it, and no OMC is required.

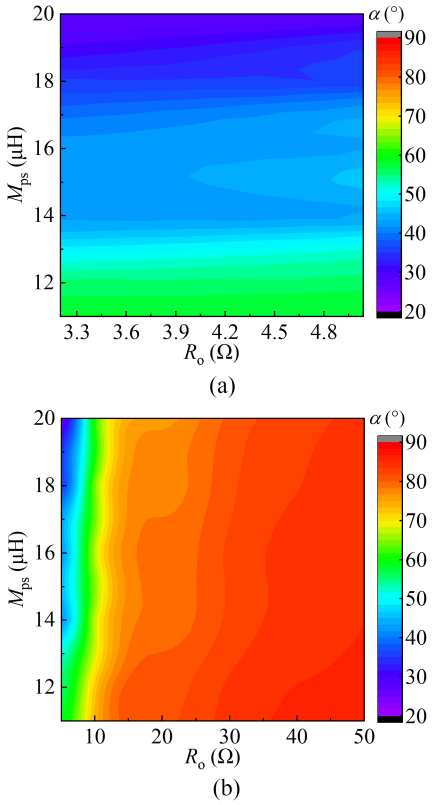

Fig. 21. Measured α when R_o and M_{ps} vary. (a) CC charging. (b) CV charging.

2) Regarding the costly problem of the designed WCS, it is analyzed as follows. First, the circuit units used to realize this article's three design goals focus on the primary side. Although this constraint condition induces a high cost for the primary side, the secondary-side cost is minimal. Then, the total cost may still not increase significantly. Second, many secondary-side modules can use one primary-side module. For example, by reasonably planning the flight path of multiple UAVs, these UAVs use one primary-side module for time-sharing charging to average the total cost, just like the EV charging station.
3) It points out many compromises in WCS design based on the literature analysis. The system's working performance should always be comprehensively evaluated from many dimensions. In other words, the more critical design goals are considered as long as system parameters are accepted. At the same time, other conditions can be reasonably relaxed considering the practical applications.
4) OMC and MFCI achieve a much better system working performance than only OMC or MFCI. For example, although OMC can realize high anti-misalignment ability, using MFCI simultaneously ensures much less charging current/voltage fluctuation when much larger horizontal misalignment occurs.

Besides, this article's research is assumed to be a preliminary attempt to achieve three design goals in one WCS only using the primary-side circuit combined with a simple secondary-side structure. The MFCI that achieves CC/CV charging and ZVS operation is an alternative to the existing primary side control methods and is suitable for most WCS. Besides, this article's reconfigurable idea can be extended to the following aspects by designing the magnetic coupler and system-level circuit, which is the work in the next stage: 1) More than two transmission channels are constructed to achieve better anti-misalignment ability. 2) Modular circuits are built to get more convenient system structure modification for some existing WCS.

VI. Conclusion

This article designs a reconfigurable WCS with a closed-loop controlled MFCI and an optimized OMC to achieve CC/CV charging, high-misalignment tolerance, and ZVS operation. First, the single-axis anti-misalignment solid ability of the magnetic coupler, which consists of the transmitter with RSS coils/ferrite cores and receiver with square coils, is verified by comparing it with some usually used magnetic couplers. Then, the designed OMC uses two orthogonally placed transmitters and one receiver to achieve a high horizontal misalignment tolerance. On this basis, the OMC's parameters are optimized using the orthogonal experimental design, and then the Ansys Maxwell simulations validate its misalignment performance. Second, the WCS's circuit structure is designed to support the OMC's feasibility combined with working principle analysis. The CC/CV charging equations and misalignment performance support the closed-loop control's feasibility. Then, the MFCI, used for output power adjustment, is illustrated from the circuit design and parameter optimization. Its working mechanism is presented from the viewpoint of magnetic potential. Third, the simulation results verify that the closed-loop controller realizes the desired three design goals. Finally, the experimental results confirm the proposed method's rationality. When the charging power is 126 W, the maximum system efficiency is 91.6%. The charging zone is an approximate circle when system efficiency decreases by 5% from the maximum value. Furthermore, the WCS suits applications that require a lightweight receiver and horizontal anti-misalignment solid ability, such as UAVs and electric scooters.

Appendix

A. Optimization of the OMC

Since the mutual inductance of OMC relates to the coil turns of two transmitters and one receiver, optimizing the coil's turn is vital for a better anti-misalignment ability. Assuming that the available coil turns of two transmitters are 12–16 and one receiver is 13–16. The OMC optimization design process is illustrated as follows.

First, the coil turns of two transmitters and one receiver are marked as factors A, B, and C. Each coil turn is marked as a level number. Then, different factors and levels are listed in Table III.

Second, based on Table III, the orthogonal experimental test is designed using the statistical package for the social science (SPSS) software, as shown in Table IV.

Third, the Ansys Maxwell simulations are done using the data in Table IV. Meanwhile, M_{as} and M_{bs} that vary less than

TABLE III
FACTORS AND LEVELS FOR THE ORTHOGONAL EXPERIMENTAL TEST

Levels \ Factors	A	B	C
1	12	12	13
2	13	13	14
3	14	14	15
4	**15**	**15**	**16**
5	16	16	

Second, based on Table A1, the orthogonal experimental test is designed using the statistical package for the social science (SPSS) software, as shown in Table A2.

TABLE IV
ORTHOGONAL EXPERIMENTAL TEST

Numbers \ Factors	A	B	C
1	1	1	1
2	1	2	3
3	1	3	1
4	1	4	2
5	1	5	4
6	2	1	2
7	2	2	2
8	2	3	4
9	2	4	1
10	2	5	3
11	3	1	4
12	3	2	1
13	3	3	3
14	3	4	3
15	3	5	2
16	4	1	3
17	4	2	4
18	4	3	2
19	**4**	**4**	**4**
20	4	5	1
21	5	1	2
22	5	2	4
23	5	3	1
24	5	4	3
25	5	5	1

5% within the 40% horizontal misalignment ratio are set as a goal to select the optimal coil turns. Then, Fig. 22 shows that NO. 19 provides the best horizontal anti-misalignment ability. Finally, the coil turns are chosen as 15 (for transmitter a), 15 (for transmitter a), and 16 (for receiver).

As a remark, it points out that 100 (= 5*5*4) simulations are required to seek the best coil turns if the enumeration method is used. However, the orthogonal experimental design only uses 25 (as listed in Table IV) simulations to obtain the optimal coil turns. The above method is much simpler than some intelligent optimization algorithms from an engineering perspective and can be used to optimize other parameters of the WCS.

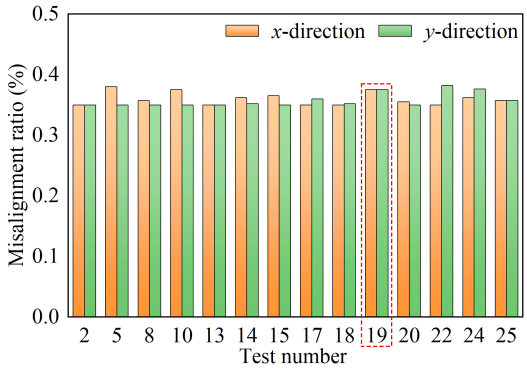

Fig. 22. Test results of the orthogonal experimental design.

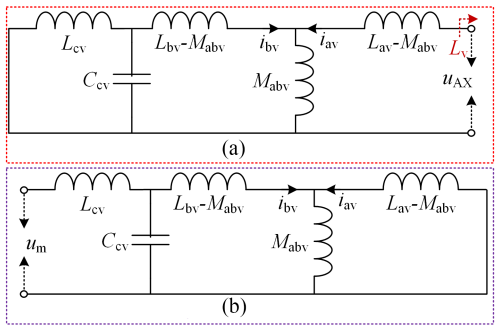

Fig. 23. MFCI's circuit model when u_{AX} and u_m work separately.

B. Circuit Parameters Design of the MFCI

The equivalent circuit model of the MFCI is further plotted in Fig. 23. When u_{AX} and u_m work separately, (A1) and (A2) can be deduced. Here, $L_{av} = L_{bv} = L_{cv} = L$

$$\dot{I}_{av1} = \frac{\dot{U}_{AX}}{j\omega L}, \dot{I}_{bv1} = 0 \tag{A1}$$

$$\dot{I}_{av2} = -\frac{M_{abv}}{L}\dot{I}_{bv2}, \dot{I}_{bv2} = -\frac{\dot{U}_m}{j\omega L}. \tag{A2}$$

Using the superposition principle, (A3) is deduced when u_{AX} and u_m work simultaneously

$$\dot{I}_{av} = \dot{I}_{av1} + \dot{I}_{av2} = \frac{\dot{U}_{AX}}{j\omega L} - \frac{M_{abv}}{L}\dot{I}_{bv2}, \dot{I}_{bv}$$

$$= \dot{I}_{bv1} + \dot{I}_{bv2} = -\frac{\dot{U}_m}{j\omega L_{cv}}. \tag{A3}$$

Then, (A4) is deduced and shows that i_{bv} leads u_m with 90°, i_{av} is antiphase with i_{bv}, and i_{bv} lags u_m with 90°

$$\dot{I}_{bv} = -\gamma\dot{I}_{av} \Rightarrow \dot{U}_m = \frac{\gamma L}{L - \gamma M_{abv}}\dot{U}_{AX} = \frac{\gamma L}{L_{av} - \gamma M_{abv}}\dot{U}_{AX}. \tag{A4}$$

Using (1)–(3) shown in Section III-B, the following equations are deduced to determine $U_{\rm dc}$:

$$U_{\rm AX} = \omega L_{\rm v} I_{\rm P} = \frac{\sqrt{2}U_{\rm bus}\omega L_{\rm v}}{\pi\sqrt{(\omega L_{\rm v})^2 + \left[R_1 + \frac{(\omega M_{\rm ps}\pi)^2}{8R_{\rm o}+R_2\pi^2}\right]^2}}. \quad \text{(A5)}$$

Based on (A4) and (A5), $U_{\rm m}$ is given by the following:

$$U_{\rm m} = \frac{\gamma L_{\rm cv}}{L_{\rm av} - \gamma M_{\rm abv}} U_{\rm AX} = \frac{\sqrt{2}U_{\rm bus}\gamma\omega L_{\rm cv}}{\pi\sqrt{[\omega(L_{\rm av} - \gamma M_{\rm abv})]^2 + \left[R_1 + \frac{(\omega M_{\rm ps}\pi)^2}{8R_{\rm o}+R_2\pi^2}\right]^2}}. \quad \text{(A6)}$$

Finally, $U_{\rm dc}$ is determined by (A7). The MFCI's circuit parameters are listed in Table I

$$U_{\rm dc} \geq \frac{\pi}{2\sqrt{2}} U_{\rm m-max}. \quad \text{(A7)}$$

C. Power Loss Analysis of MFCI

The MFCI's power loss mainly occurs at the following parts: the full-bridge inverter, *LC* filter, and transformer.

1) The power loss of the H-bridge inverter. It consists of MOSFETs' conduction and switching loss and their antiparallel diodes. Each part of this power loss is calculated based on the inherent parameters of the inverter.
   a) The output current of the inverter $i_{\rm m}$, conduction time, and drain–source ON-state resistance $r_{\rm m}$ calculate the conduction loss of MOSFETs. Its expression is given by (A8). δ is the dead time of two pulsewidth modulation signals, a small value assumes as zero

$$P_{\rm mos} = \frac{2}{\pi} I_{\rm m}^2 r_{\rm m}\left[\pi - \delta + \frac{1}{2}(\sin\alpha - \sin(\alpha + 2\delta))\right] \approx 2I_{\rm m}^2 r_{\rm m}. \quad \text{(A8)}$$

   b) The conduction loss of the antiparallel diodes is generated during the period of δ, when MOSFETs are switching. Its expression is given by (A9). $V_{\rm if}$ and $r_{\rm id}$ are antiparallel diodes' forward voltage drop and the equivalent ON-state resistance

$$P_{\rm diode} = \frac{2\sqrt{2}}{\pi} V_{\rm if} I_{\rm m}\left(\sin\left(\frac{\alpha}{2} + \delta\right) - \sin\frac{\alpha}{2}\right) + \frac{2}{\pi} I_{\rm m}^2 r_{\rm id}\left[\delta + \frac{1}{2}(\sin(\alpha + 2\delta) - \sin\alpha)\right] \approx 0. \quad \text{(A9)}$$

   c) The switching power loss of the inverter, including the MOSFETs and their antiparallel diodes, is given by (A10). $E_{\rm on}$ and $E_{\rm off}$ are the turn-ON and turn-OFF energy losses of the MOSFETs; $V_{\rm D}$ and $I_{\rm D}$ are the drain–source voltage and source current of the MOSFETs; $Q_{\rm D}$ and $I_{\rm R\_D}$ are the reverse recovery charge and reference current of the diode

$$P_{\rm sw} = 2\sqrt{2} V_{\rm dc} I_{\rm m}\left|\cos\frac{\alpha}{2}\right|\left(\frac{E_{\rm on} + E_{\rm off}}{V_{\rm D} I_{\rm D}} + \frac{Q_{\rm D}}{I_{\rm R\_D}}\right) f. \quad \text{(A10)}$$

   d) In the above analysis, the total power loss of the inverter is given by the following:

$$P_{\rm inv} = P_{\rm mos} + P_{\rm diode} + P_{\rm sw} = 2I_{\rm m}^2 r_{\rm m} + 2\sqrt{2} V_{\rm dc} I_{\rm m}\left|\cos\frac{\alpha}{2}\right| \times \left(\frac{E_{\rm on} + E_{\rm off}}{V_{\rm D} I_{\rm D}} + \frac{Q_{\rm D}}{I_{\rm R\_D}}\right) f. \quad \text{(A11)}$$

2) *Power loss calculation for the transformer:* The equation is expressed as (A11). $V_{\rm av}$ and $V_{\rm bv}$ are the core volumes used by the primary and secondary sides of the transformer. $B_{\rm ma}$ and $B_{\rm mb}$ are the peak magnetic flux density's primary and secondary sides. The Steinmetz coefficients k, c, and e related to the core material are obtained from manufacturer datasheets. Besides, some low-power loss ferrite cores, such as PC44 and PC95, are potential candidates for WCS. The transformer in this article uses MnZn ferrite cores, PC95. The coefficients of this core material are $k = 0.00925$, $c = 1.86$, and $e = 3.03$

$$P_{\rm mag} = \underbrace{I_{\rm av}^2 R_{\rm av} + I_{\rm bv}^2 R_{\rm bv}}_{\rm Coilloss} + \underbrace{V_{\rm av} k f^c B_{\rm ma}^e + V_{\rm bv} k f^c B_{\rm mb}^e}_{\rm Coreloss}. \quad \text{(A12)}$$

3) *Power loss calculation for the LC filter:* The equation is expressed as (A13). Note: The parameters related to the ferrite core are the same as (A12)

$$P_{\rm fil} = \underbrace{I_{\rm v}^2 R_{\rm lv}}_{\rm Coilloss} + \underbrace{V_{\rm ac} k f^c B_{\rm mc}^e}_{\rm Coreloss} + \underbrace{I_{\rm c}^2 R_{\rm cv}}_{\rm Capacitorloss}, I_{\rm c} = I_{\rm v} - I_{\rm bv}. \quad \text{(A13)}$$

4) The power loss calculation for the MFCI is given by the following:

$$P_{\rm MFCI} = P_{\rm inv} + P_{\rm fil} + P_{\rm mag}. \quad \text{(A14)}$$

REFERENCES

[1] S. Y. Hui, "Planar wireless charging technology for portable electronic products and Qi," *Proc. IEEE*, vol. 101, no. 6, pp. 1290–1301, Jun. 2013.

[2] C. Wei, X. Liu, S. Wu, X. Chen, W. Chai, and S. Yang, "A misalignment tolerance and lightweight wireless charging system via reconfigurable capacitive coupling for unmanned aerial vehicle applications," *IEEE Trans. Power Electron.*, vol. 38, no. 1, pp. 22–26, Jan. 2023.

[3] Z. Luo, Y. Zhao, M. Xiong, X. Wei, and H. Dai, "A self-tuning LCC/LCC system based on switch-controlled capacitors for constant-power wireless electric vehicle charging," *IEEE Trans. Ind. Electron.*, vol. 70, no. 1, pp. 709–720, Jan. 2023.

[4] J. Hou, Q. Chen, X. Ren, X. Ruan, S. C. Wong, and C. K. Tse, "Precise characteristics analysis of series/series-parallel compensated contactless resonant converter," *IEEE J. Emerg. Sel. Topics Power Electron.*, vol. 3, no. 1, pp. 101–110, Mar. 2015.

[5] Y. H. Sohn, B. H. Choi, E. S. Lee, G. C. Lim, G. H. Cho, and C. T. Rim, "General unified analyses of two-capacitor inductive power transfer systems: Equivalence of current-source SS and SP compensations," *IEEE Trans. Power Electron.*, vol. 30, no. 11, pp. 6030–6045, Nov. 2015.

[6] J. Cai, X. Wu, P. Sun, Q. Deng, J. Sun, and H. Zhou, "Design of constant-voltage and constant-current output modes of double-sided LCC inductive power transfer system for variable coupling conditions," *IEEE Trans. Power Electron.*, to be published, doi: 10.1109/TPEL.2022.3226756.

[7] J. Lu, G. Zhu, D. Lin, Y. Zhang, J. Jiang, and C. C. Mi, "Unified load independent ZPA analysis and design in CC and CV modes of higher order resonant circuits for WPT systems," *IEEE Trans. Transp. Electrific.*, vol. 5, no. 4, pp. 977–987, Dec. 2019.

[8] R. Mai, Y. Chen, Y. Li, Y. Zhang, G. Cao, and Z. He, "Inductive power transfer for massive electric bicycles charging based on hybrid topology switching with a single inverter," *IEEE Trans. Power Electron.*, vol. 32, no. 8, pp. 5897–5906, Aug. 2017.

[9] Z. Huang, D. Wang, and X. Qu, "A novel IPT converter with current-controlled semi-active rectifier for efficiency enhancement throughout supercapacitor charging process," *IEEE J. Emerg. Sel. Topics Power Electron.*, vol. 10, no. 2, pp. 2201–2209, Apr. 2022.

[10] M. Fan, L. Shi, Z. Yin, and Y. Li, "A novel pulse density modulation with semi-bridgeless active rectifier in inductive power transfer system for rail vehicle," *CES Trans. Elect. Mach. Syst.*, vol. 1, no. 3, pp. 397–404, Dec. 2017.

[11] G. R. Kalra, B. S. Riar, and D. J. Thrimawithana, "An integrated boost active bridge based secondary inductive power transfer converter," *IEEE Trans. Power Electron.*, vol. 35, no. 12, pp. 12716–12727, Dec. 2020.

[12] Z. Liu, L. Wang, Y. Guo, and S. Li, "Primary-side linear control for constant current/voltage charging of the wireless power transfer system based on the LCC-N compensation topology," *IEEE Trans. Ind. Electron.*, vol. 69, no. 9, pp. 8895–8904, Sep. 2022.

[13] L. Wu, B. Zhang, and J. Zhou, "Efficiency improvement of the parity-time-symmetric wireless power transfer system for electric vehicle charging," *IEEE Trans. Power Electron.*, vol. 35, no. 11, pp. 12497–12508, Nov. 2020.

[14] J. M. Miller, O. C. Onar, and M. Chinthavali, "Primary-side power flow control of wireless power transfer for electric vehicle charging," *IEEE J. Emerg. Sel. Topics Power Electron.*, vol. 3, no. 1, pp. 147–162, Mar. 2015.

[15] Y. Jiang, L. Wang, Y. Wang, J. Liu, X. Li, and G. Ning, "Analysis, design, and implementation of accurate ZVS angle control for EV battery charging in wireless high-power transfer," *IEEE Trans. Ind. Electron.*, vol. 66, no. 5, pp. 4075–4085, May 2019.

[16] N. Fu, J. Deng, Z. Wang, and D. Chen, "An LCC–LCC compensated WPT system with switch-controlled capacitor for improving efficiency at wide output voltages," *IEEE Trans. Power Electron.*, vol. 38, no. 7, pp. 9183–9194, Jul. 2023.

[17] Y. Li et al., "Extension of ZVS region of series-series WPT systems by an auxiliary variable inductor for improving efficiency," *IEEE Trans. Power Electron.*, vol. 36, no. 7, pp. 7513–7525, Jul. 2021.

[18] J. Li, C. Zhu, J. Xie, F. Lu, and X. Zhang, "Design and implementation of high-misalignment tolerance WPT system for underwater vehicles based on a variable inductor," *IEEE Trans. Power Electron.*, to be published, doi: 10.1109/TPEL.2023.3267104.

[19] Y. Zhang, Q. Chen, and L. Cheng, "A high-power controllable reactor based on transformer magnetic flux compensation," in *Proc. Int. Conf. Elect. Mach. Syst.*, 2007, pp. 1286–1290.

[20] S. Kim, G. A. Covic, and J. T. Boys, "Tripolar pad for inductive power transfer systems for EV charging," *IEEE Trans. Power Electron.*, vol. 32, no. 7, pp. 5045–5057, Jul. 2017.

[21] V. B. Vu et al., "Operation of inductive charging systems under misalignment conditions: A review for electric vehicles," *IEEE Trans. Transp. Electron.*, vol. 9, no. 1, pp. 1857–1887, Mar. 2023.

[22] A. Zaheer, G. A. Covic, and D. Kacprzak, "A bipolar pad in a 10-kHz 300-W distributed IPT system for AGV applications," *IEEE Trans. Ind. Electron.*, vol. 61, no. 7, pp. 3288–3301, Jul. 2014.

[23] S. Kim, G. A. Covic, and J. T. Boys, "Comparison of tripolar and circular pads for IPT charging systems," *IEEE Trans. Power Electron.*, vol. 33, no. 7, pp. 6093–6103, Jul. 2018.

[24] J. Mai, Y. Wang, Y. Yao, M. Sun, and D. Xu, "High-misalignment tolerant IPT systems with solenoid and double D-pads," *IEEE Trans. Ind. Electron.*, vol. 69, no. 4, pp. 3527–3535, Apr. 2022.

[25] Y. Chen, R. Mai, Y. Zhang, M. Li, and Z. He, "Improving misalignment tolerance for IPT system using a third-coil," *IEEE Trans. Power Electron.*, vol. 34, no. 4, pp. 3009–3013, Apr. 2019.

[26] Z. Yuan, M. Saeedifard, C. Cai, Q. Yang, P. Zhang, and H. Lin, "A misalignment tolerant design for a dual-coupled LCC-S-compensated WPT system with load-independent CC output," *IEEE Trans. Power Electron.*, vol. 37, no. 6, pp. 7480–7492, Jun. 2022.

[27] Y. Chen et al., "A hybrid inductive power transfer system with misalignment tolerance using quadruple-D quadrature pads," *IEEE Trans. Power Electron.*, vol. 35, no. 6, pp. 6039–6049, Jun. 2020.

[28] Y. Yao, Y. Wang, X. Liu, K. Lu, and D. Xu, "Analysis and design of an S/SP compensated IPT system to minimize output voltage fluctuation versus coupling coefficient and load variation," *IEEE Trans. Veh. Technol.*, vol. 67, no. 10, pp. 9262–9272, Oct. 2018.

[29] J. Hou, Q. Chen, Z. Zhang, S.-C. Wong, and C. K. Tse, "Analysis of output current characteristics for higher order primary compensation in inductive power transfer systems," *IEEE Trans. Power Electron.*, vol. 33, no. 8, pp. 6807–6821, Aug. 2018.

[30] L. Zhao, D. J. Thrimawithana, U. K. Madawala, A. P. Hu, and C. C. Mi, "A misalignment-tolerant series-hybrid wireless EV charging system with integrated magnetics," *IEEE Trans. Power Electron.*, vol. 34, no. 2, pp. 1276–1285, Feb. 2019.

[31] Y. Chen, B. Yang, Z. Kou, Z. He, G. Cao, and R. Mai, "Hybrid and reconfigurable IPT systems with high-misalignment tolerance for constant-current and constant-voltage battery charging," *IEEE Trans. Power Electron.*, vol. 33, no. 10, pp. 8259–8269, Oct. 2018.

[32] H. Feng, T. Cai, S. Duan, X. Zhang, H. Hu, and J. Niu, "A dual-side detuned series-series compensated resonant converter for a wide charging region in a wireless power transfer system," *IEEE Trans. Ind. Electron.*, vol. 65, no. 3, pp. 2177–2188, Mar. 2018.

[33] J. Yang, X. Zhang, K. Zhang, X. Cui, C. Jiao, and X. Yang, "Design of LCC-S compensation topology and optimization of misalignment tolerance for inductive power transfer," *IEEE Access*, vol. 8, pp. 191309–191318, 2020.

[34] Z. Liu, M. Su, Q. Zhu, L. Zhao, and A. P. Hu, "A dual-frequency tuning method for improved coupling tolerance of wireless power transfer system," *IEEE Trans. Power Electron.*, vol. 36, no. 7, pp. 7360–7365, Jul. 2021.

[35] C. Xia, W. Wang, S. Ren, X. Wu, and Y. Sun, "Robust control for inductively coupled power transfer systems with coil misalignment," *IEEE Trans. Power Electron.*, vol. 33, no. 9, pp. 8110–8122, Sep. 2018.

[36] C. Xia, W. Wang, S. Ren, X. Wu, and Y. Sun, "Robust control for inductively coupled power transfer systems with coil misalignment," *IEEE Trans. Power Electron.*, vol. 33, no. 9, pp. 8110–8122, Sep. 2018.

[37] J. Chen et al., "Free-positioning wireless power transfer system based on one-to-multiple topology," *IEEE Trans. Power Electron.*, vol. 35, no. 10, pp. 9959–9964, Oct. 2020.

[38] C. Cai, J. Wang, F. Zhang, X. Liu, P. Zhang, and Y.-G. Zhou, "A multichannel wireless UAV charging system with compact receivers for improving transmission stability and capacity," *IEEE Syst. J.*, vol. 16, no. 1, pp. 997–1008, Mar. 2022.

[39] C. Cai, X. Liu, S. Wu, X. Chen, W. Chai, and S. Yang, "A misalignment tolerance and lightweight wireless charging system via reconfigurable capacitive coupling for unmanned aerial vehicle applications," *IEEE Trans. Power Electron.*, vol. 38, no. 1, pp. 22–26, Jan. 2023.

[40] Y. Zhang et al., "Misalignment-tolerant dual-transmitter electric vehicle wireless charging system with reconfigurable topologies," *IEEE Trans. Power Electron.*, vol. 37, no. 8, pp. 8816–8819, Aug. 2022.

[41] D. Ahn and S. Hong, "Effect of coupling between multiple transmitters or multiple receivers on wireless power transfer," *IEEE Trans. Ind. Electron.*, vol. 60, no. 7, pp. 2602–2613, Jul. 2013.

[42] Y. Zhang, Z. Yan, T. Kan, X. Zeng, S. Chen, and C. C. Mi, "Modeling and analysis of a strongly coupled series-parallel-compensated wireless power transfer system," *IEEE J. Emerg. Sel. Topics Power Electron.*, vol. 7, no. 2, pp. 1364–1370, Jun. 2019.

[43] S. Huh et al., "Transmitter coils selection method for wireless power transfer system with multiple transmitter coils and single receiver coil," *IEEE Trans. Power Electron.*, vol. 38, no. 3, pp. 4092–4109, Mar. 2023.

[44] D. H. Kim, S. Kim, S. W. Kim, J. Moon, I. Cho, and D. Ahn, "Coupling extraction and maximum efficiency tracking for multiple concurrent transmitters in dynamic wireless charging," *IEEE Trans. Power Electron.*, vol. 35, no. 8, pp. 7853–7862, Aug. 2020.

[45] S. Huh and D. Ahn, "Two-transmitter wireless power transfer with optimal activation and current selection of transmitters," *IEEE Trans. Power Electron.*, vol. 33, no. 6, pp. 4957–4967, Jun. 2018.

[46] R. Mai, Z. Yan, Y. Chen, S. Liu, and Z. He, "A hybrid transmitter-based efficiency improvement controller with full-bridge dual resonant tank for misalignment condition," *IEEE Trans. Power Electron.*, vol. 36, no. 7, pp. 1124–1135, Jan. 2020.

[47] T. Feng, Y. Sun, Y. Feng, and X. Dai, "A tripolar plane-type transmitter for three-dimensional omnidirectional wireless power transfer," *IEEE Trans. Ind. Appl.*, vol. 58, no. 1, pp. 1254–1267, Jan./Feb. 2022.

[48] C. Cai, J. Wang, H. Nie, P. Zhang, Z. Lin, and Y. G. Zhou, "Effective-configuration WPT systems for drones charging area extension featuring quasi-uniform magnetic coupling," *IEEE Trans. Transp. Electrific.*, vol. 6, no. 3, pp. 920–934, Sep. 2020.

[49] S. A. A. Mahmud, I. Panhwar, and P. Jayathurathnage, "Large-area free-positioning wireless power transfer to movable receivers," *IEEE Trans. Ind Electron.*, vol. 69, no. 12, pp. 12807–12816, Dec. 2022.

[50] G. Ning, K. Zhao, and M. Fu, "A passive current sharing method for multi-transmitter inductive power transfer systems," *IEEE Trans. Ind. Electron.*, vol. 69, no. 5, pp. 4617–4626, May 2022.
[51] Y. Li, R. Mai, L. Lu, and Z. He, "Active and reactive currents decomposition-based control of angle and magnitude of current for a parallel multi-inverter IPT system," *IEEE Trans. Power Electron.*, vol. 32, no. 2, pp. 1602–1614, Feb. 2017.
[52] Q. Deng, J. Liu, D. Czarkowski, W. Hu, and H. Zhou, "An inductive power transfer system supplied by a multiphase parallel inverter," *IEEE Trans. Ind. Electron.*, vol. 64, no. 9, pp. 7039–7048, Sep. 2017.
[53] H. Wang, Y. Chen, Y. Liu, J. Afsharian, and Z. Yang, "A passive current sharing method with common inductor multiphase LLC resonant converter," *IEEE Trans. Power Electron.*, vol. 32, no. 9, pp. 6994–7010, Sep. 2017.

Zhenjie Li (Member, IEEE) received the B.S. degree in measurement and control technology and instruments from the School of Measurement and Control Technology and Communication Engineering, Harbin University of Science and Technology, Harbin, China, in 2012, and the M.S. degree in instrument science and technology, and Ph.D. degree electrical engineering from the School of Electrical Engineering and Automation, Harbin Institute of Technology, in 2014 and 2020, respectively.

He has been an Associate Professor with the College of Computer and Control Engineering, Northeast Forestry University, since 2020. His research interests include designing and controlling the wireless charging system with multiple applications and power levels. He has published a highly cited ESI paper in IEEE TRANSACTIONS ON POWER ELECTRONICS.

Jiafang He received the B.S. degree in electrical engineering and automation from the College of Mechanical and Electrical Engineering, Northeast Forestry University, Harbin, China, in 2021. He is currently working toward the M.S. degree in control engineering from Northeast Forestry University.

His current research interests include magnetic coupler design and the charging control for the wireless charging system used for EVs.

Yusheng Huo received the B.S. degree in electrical engineering and automation from the College of Mechanical and Electrical Engineering, Northeast Forestry University, Harbin, China, in 2021. He is currently working toward the M.S. degree in control engineering from Northeast Forestry University.

His current research interests include designing the circuit topology, resonant converters, and the charging controller for the wireless charging system used for UAVs.

Mingfei Ban (Member, IEEE) received the B.S., M.S., and Ph.D. degrees in electrical engineering from the Harbin Institute of Technology, Harbin, China, in 2011, 2013, and 2019, respectively.

He was a visiting Ph.D. student with the Illinois Institute of Technology. He has been an Associate Professor with the College of Computer and Control Engineering, Northeast Forestry University. His research interests include electric vehicles, sustainable energy, and microgrids.

Yiqi Liu (Member, IEEE) received the B.S. degree from the Northeast Agriculture University, Harbin, China, in 2009, the M.S. degree from the Tianjin University of Technology, Tianjin, China, in 2012, and the Ph.D. degree from the Harbin Institute of Technology, Harbin, China, in 2016, all in electrical engineering.

From 2013 to 2015, he was a Visiting Ph.D. student with the Center for Ultra-Wide-Area Resilient Electric Energy Transmission Networks, University of Tennessee, Knoxville, TN, USA, with support from CSC. He joined the Northeast Forestry University, Harbin, China, in 2016, working as an Associate Professor. His research interests include power electronics for renewable energy sources, multilevel converters, high-voltage direct-current technology, dc microgrids, energy conversion, and wireless power transfer systems.

Jiuqing Liu received the B.S. and Ph.D. degrees in mechanical design and theory from the College of Mechanical and Electrical Engineering, Northeast Forestry University, Harbin, China, in 1994 and 2005, respectively.

He has been a Professor with the College of Mechanical and Electrical Engineering, Northeast Forestry University, since 2009. His research interests include forestry and woodworking machinery design and manufacturing, forest information collection, robot structure and control, and forestry artificial intelligence.